
Article

Not peer-reviewed version

Obtention and Characterization of TiO₂-Folic Acid-ZnPc Semiconductor Nanoparticles for Photodynamic Therapy Against Glioma Cells

[Citlali Ekaterina Rodríguez-Pérez](#) , Sonia Rodríguez-García , Ma. Elena Manríquez-Ramírez ,
[A. Martín Ortiz-Torres](#) , [Francisco Tzompantzi-Morales](#) , [Emma Ortiz-Islands](#) *

Posted Date: 2 July 2025

doi: 10.20944/preprints202507.0220.v1

Keywords: nanoparticles; TiO₂; photosensitizers; semiconductors; photodynamic therapy; folic acid; zinc phthalocyanine; glioma cells



Preprints.org is a free multidisciplinary platform providing preprint service that is dedicated to making early versions of research outputs permanently available and citable. Preprints posted at Preprints.org appear in Web of Science, Crossref, Google Scholar, Scilit, Europe PMC.

Copyright: This open access article is published under a Creative Commons CC BY 4.0 license, which permit the free download, distribution, and reuse, provided that the author and preprint are cited in any reuse.

Disclaimer/Publisher's Note: The statements, opinions, and data contained in all publications are solely those of the individual author(s) and contributor(s) and not of MDPI and/or the editor(s). MDPI and/or the editor(s) disclaim responsibility for any injury to people or property resulting from any ideas, methods, instructions, or products referred to in the content.

Article

Obtention and Characterization of TiO₂-Folic Acid-ZnPc Semiconductor Nanoparticles for Photodynamic Therapy Against Glioma Cells

C. Ekaterina Rodríguez-Pérez ¹, Sonia Rodríguez-García ^{1,2}, Ma. Elena Manríquez-Ramírez ³, A. Martín Ortiz-Torres ⁴, Francisco Tzompantzi-Morales ⁵ and Emma Ortiz-Islas ^{1,*}

¹ Laboratorio de Neurofarmacología Molecular y Nanotecnología, Instituto Nacional de Neurología y Neurocirugía, Insurgentes Sur 3877, La Fama 14269, Tlalpan CDM, México

² Facultad de Psicología-UNAM, Universidad 3004, Copilco 04510, Ciudad Universitaria CDMX, México

³ Laboratorio de investigación en nanomateriales y energías limpias, ESIQIE-IPN, Instituto Politécnico Nacional, Lindavista 07700, Gustavo A. Madero CDMX, México

⁴ Instituto de Ingeniería de la UNAM, Circuito Escolar s/n, Ciudad Universitaria 04510, CDMX; México

⁵ Departamento de Química, Universidad Autónoma Metropolitana-Iztapalapa, San Rafael Atlixco 186, Vicentina 09340, Iztapalapa CDMX, México

* Correspondence: emma.ortiz@innn.edu.mx

Abstract

Background/Objectives: This paper reports the synthesis of TiO₂ nanoparticles, their functionalization with folic acid (FA), and loading with zinc phthalocyanine (ZnPc) to develop photosensitizers for photodynamic therapy applications against glioma cells. **Methods:** TiO₂, TiO₂-FA, and TiO₂-FA-ZnPc nanoparticles were obtained via the sol-gel process, involving hydrolysis and condensation of titanium (IV) isopropoxide. During these steps, FA and ZnPc were incorporated into the TiO₂ network in vitro. The resulting TiO₂-based materials were characterized using transmission and scanning electron microscopy, X-ray diffraction, Raman and UV-Vis spectroscopy, thermogravimetry, and nitrogen adsorption-desorption measurements. An *in vitro* study was also conducted using the 1,3-diphenylisobenzofuran (DPBF) probe to determine ROS generation by TiO₂. To achieve this, a 40-ppm solution was irradiated with UV light in the presence of each TiO₂ system. Biological assays involved evaluating the viability of LN18 and U251 (human glioblastoma) cells incubated with different TiO₂ systems, both with and without UV light irradiation. **Results:** Although TiO₂ retained its primary characteristics, such as a large surface area (around 600–700 m²/g), mesoporous structure (approximately 4–5 nm pore size), mixed anatase-amorphous morphology, and a bandgap of ~3.46 eV; each titania sample also displayed unique features. The UV-Vis spectrum of TiO₂-FA-ZnPc exhibited additional absorption bands in the visible range (600–700 nm). The characteristic DPBF absorption signal at 410 nm decreased gradually with irradiation time. Complete degradation of DPBF occurred in 10 minutes with TiO₂, 12 minutes with TiO₂-FA, and 14 minutes with TiO₂-FA-ZnPc. LN18 and U251 cells were not damaged by the presence of the materials alone at concentrations <100 µg/mL, in contrast to cells irradiated with UV light. **Conclusions:** Biocompatible materials with phototoxicity under UV light were successfully synthesized, making them promising candidates for application in photodynamic therapy.

Keywords: nanoparticles; TiO₂; photosensitizers; semiconductors; photodynamic therapy; folic acid; zinc phthalocyanine; glioma cells

1. Introduction



Titanium dioxide (TiO_2), better known as titania, is a metal oxide with a wide range of applications, mainly in photo-processes due to its semiconducting properties. Titania naturally occurs in three crystalline phases, named anatase, rutile, and brookite, each with distinct physicochemical properties, crystalline structures, and morphology [1]. TiO_2 is not only widely used as a photocatalyst for the degradation of organic compounds in wastewater but also in hydrogen production via water splitting and in redox reactions to obtain high-value products [2-4]. As a semiconductor, TiO_2 is photoexcited upon exposure to ultraviolet light and/or sunlight. During this process, it absorbs photons with sufficient energy (≤ 390 nm) and transfers electrons from its valence band to its conduction band, generating holes (h^+) and electrons (e^-), respectively. Thus, oxidation/reduction photocatalytic reactions of surface-adsorbed molecules can occur on the TiO_2 surface [5]. These surface charges react with water molecules and molecular oxygen, leading to the formation of highly reactive oxygen species (ROS), such as hydroxyl radicals ($\bullet\text{OH}$), superoxide anions (O_2^-), and hydrogen peroxide (H_2O_2). Hydroxyl radicals can react with dyes, pharmaceutical compounds, and pesticide contaminants in wastewater to form carbon dioxide and water [6-8]. This photodegradation process is widely used for wastewater and air remediation [9].

In addition to its photocatalytic properties, TiO_2 exhibits other favorable features, such as a large surface area, mesoporous structure, high stability, low toxicity, and good biocompatibility [10-12]. These properties make TiO_2 suitable for biomedical applications. TiO_2 has been used as an implant material, biosensor, drug delivery vehicle, antimicrobial agent, and in tissue engineering. Due to its ability to generate ROS, TiO_2 has also been explored for cancer therapy, particularly photodynamic therapy (PDT) [13-15]. The ROS generated by irradiated TiO_2 can destroy cancer cells by damaging key cellular components such as DNA, lipids, and membranes, and by inducing various cell death mechanisms, including apoptosis, necrosis, and autophagy. TiO_2 has been studied in PDT against cancer cell lines, including breast cancer (4T1), adherent epithelial (KB), glioblastoma, non-small cell lung cancer (A549), cervical cancer (HeLa), breast epithelial (MCF7), breast cancer (MDA-MB-231), and non-small cell lung cancer (NSCLC) [16-20]. Compared to conventional cancer treatments, PDT is considered a non-invasive approach, offering reduced toxicity, short treatment durations, and clinical approval. PDT can also be combined with other therapies, such as surgery, chemotherapy, and radiotherapy.

PDT relies on three key components: a suitable light source (UV and/or visible), a photosensitizer (PS) that absorbs light at these wavelengths, and sufficient molecular oxygen [21,22]. In practice, the PS is administered (orally, subcutaneously, or intravenously) and accumulates in the tumor. Once localized, it is irradiated to induce charge transfer from its ground state to form excited states [21,22]. As reported in the literature, several events may occur during this excitation process (see Scheme I) [23]: (1) the PS transitions from its ground state to an excited singlet state (PSES), (2) the singlet state may return to the ground state by emitting absorbed energy as fluorescence or heat; or (3) it may interconvert into a longer-lived triplet state (PSET). The PSET species can generate two types of reactive species leading to two types of photo-oxidative reactions (Scheme I): in a type I reaction, transfer of a proton or electron generates excited PSET and radicals that react with oxygen to form peroxides, hydroxyl radicals, and superoxide ions. In a type II reaction, energy is transferred to molecular oxygen to form singlet oxygen. The transfer of energy from PSET to biological substrates or oxygen leads to ROS production, which is cytotoxic and induces apoptosis or necrosis [24].

Currently, various compounds are used as PSs, including dyes, drugs, synthetic chemicals, and natural products, and have been grouped into first, second, and third-generation categories [25,26]. In the early application of PDT, hematoporphyrin (HpD) was broadly used as a photosensitizer agent, thus giving rise to the first generation of PSs [21]. However, it had drawbacks including a short half-life and low efficacy in deep tissues, prompting the development of second-generation PSs with improved properties and reduced toxicity. Most second-generation PSs are heterocyclic porphyrins, such as bacteriochlorins, bacterial chlorophyll, chlorins, protoporphyrins, phthalocyanines, and their derivatives [21]. Some non-porphyrin PSs include 5-aminolevulinic acid, curcumin, quinone, phenothiazine, and psoralen. Although less toxic, many second-generation PSs exhibit poor water solubility and low tumor selectivity. Third-generation PSs aims to increase cancer-cell selectivity and minimize damage to healthy tissue [27]. To achieve this, second-generation PSs

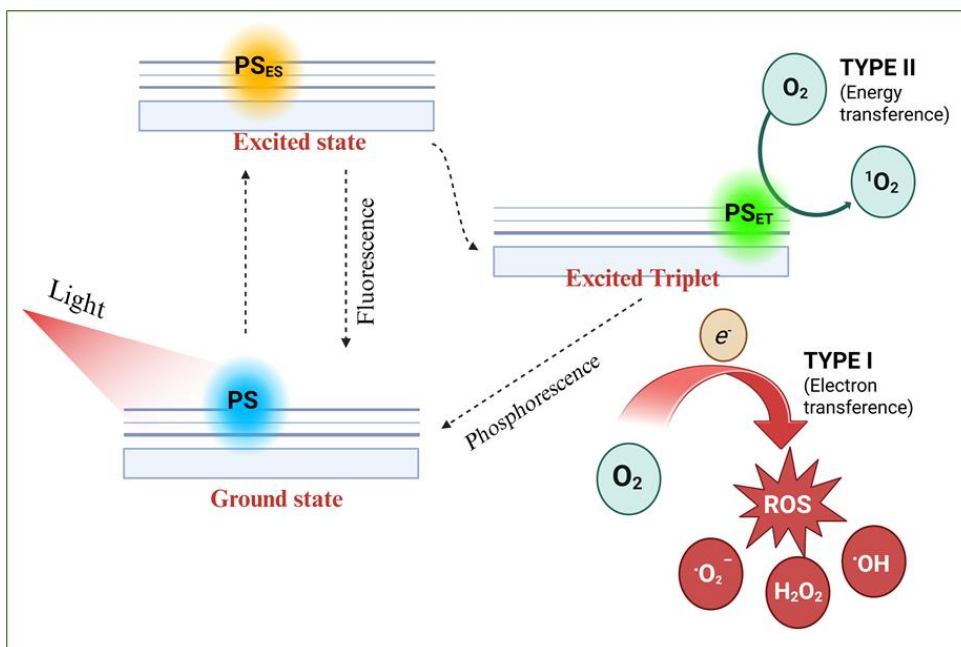
are modified by attaching bio-specific molecules or carriers to enhance biocompatibility and targeting ability.

The use of nanomaterials as PS carriers or PSs themselves is a promising strategy, offering high biocompatibility due to their generally low toxicity [28]. Additional advantages include high loading efficiency and controlled PS release due to their large surface area, improved solubility by reducing aggregation, autonomous ROS generation, enhanced phototherapeutic window for deeper tissue penetration, and surface functionalization with targeting ligands to deliver PSs specifically to tumor cells [28,29]. Many cancer cells overexpress specific surface receptors, allowing nanomaterials to be functionalized with ligands targeting these receptors [30]. Examples of such ligands include folate, CD 44 receptor, monoclonal antibodies, transferrin, and other antibodies. This selective accumulation increases PS delivery to tumor cells and spares healthy tissue from toxic effects. Nanomaterials for PDT are classified into two categories: organic (e.g., liposomes, dendrimers, polymeric nanoparticles) and inorganic (e.g., silica, magnetic materials, quantum dots, metal oxides, and metals) [29].

According to the World Health Organization (WHO), glioblastoma is classified as a grade IV cancer, the most malignant form [31]. Although rare, it has a median survival of just 15 months due to high histological heterogeneity, invasiveness, rapid proliferation, and angiogenesis. Current treatment involves maximal surgical resection followed by temozolomide (TMZ) and radiotherapy [32]. Despite these approaches, glioma patients have a poor prognosis with relatively short survival, and the blood-brain barrier (BBB) prevents many chemotherapeutic agents from reaching the tumor. Therefore, developing new or improved therapeutic strategies is critically important.

Phthalocyanines (Pc), second-generation PSs, are aromatic heterocycles composed of four isoindole rings linked by nitrogen atoms. Their properties have been enhanced by adding substituents to the rings or incorporating a silicon atom or metals such as zinc or aluminum [33]. Zinc phthalocyanine (ZnPc) contains zinc metal ions in its core and exhibits desirable properties, including efficient 1O_2 generation, high therapeutic efficacy, low skin photosensitivity, and ROS production. However, ZnPc is not yet clinically approved due to its poor solubility and tendency to aggregate in solution.

In this work, we obtained, characterized, and applied TiO_2 semiconductor nanoparticles functionalized with folate groups and loaded with ZnPc to develop selective photosensitizers for glioma cells. The aim is to stabilize ZnPc on a functionalized TiO_2 -FA support that also generates ROS and enables targeted delivery. This strategy produces a composite that combines the beneficial properties of TiO_2 and ZnPc. The samples were synthesized using the sol-gel method, which enables the incorporation of both folic acid and ZnPc in vitro. In vitro singlet oxygen studies using the 1,3-diphenylisobenzofuran (DPBF) test showed the disappearance of the 410 nm band with increasing UV irradiation time and exposure to different TiO_2 systems. LN18 and U251 cells were not damaged by the presence of these materials at low concentrations compared to cells irradiated with UV light alone.



Scheme 1. Schematic photodynamic reactions mechanisms (type I and II) upon light irradiation on a photosensitizer.

2. Materials and Methods

2.1. Samples Preparation

Chemical substances: tert-butyl alcohol [Sigma-Aldrich, ≥99%], titanium (IV) isopropoxide [Sigma-Aldrich, 97%], folic acid (FA) [Sigma-Aldrich, ≥97%], zinc phthalocyanine (ZnPc) [Aldrich, 97%], deionized water [Meyer], 1,3-diphenylisobenzofuran (BFS) [Aldrich, 97%]

Three samples were prepared via the sol-gel process: the first was TiO₂, the second was TiO₂ functionalized with folic acid (TiO₂-FA), and the third was loaded with zinc phthalocyanine on functionalized TiO₂-FA (TiO₂-FA-ZnPc). The molar ratios used were alkoxide: water (1:16) and alkoxide: alcohol (1:8). 0.5 g was added from both FA and ZnPc.

2.1.1. TiO₂

185 mL of tert-butyl alcohol was mixed with 72 mL of deionized water and stirred for 30 min. Then, 78 mL of titanium (IV) isopropoxide was slowly added dropwise over approximately 4 h. After the full addition of the alkoxide, the final mixture was stirred for 24 h. After, excess water and alcohol were removed by centrifugation. Finally, the sample was dried at 60 °C for 12 h.

2.1.2. TiO₂-FA

0.5 g of folic acid was dissolved in 185 mL of tert-butyl alcohol and 72 mL of water. Then, 78 mL of titanium (IV) isopropoxide was added slowly (dropwise). After the full addition, the mixture was stirred for 24 h. The excess solvents were removed by centrifugation, and the final sample was dried at 60 °C for 12 h.

2.1.3. TiO₂-AF-ZnPc

0.5 g of folic acid was dissolved in 92.6 mL of tert-butyl alcohol and 36 mL of water and stirred for 30 min. Then, 78 mL of titanium (IV) isopropoxide was added slowly (dropwise). After the full addition, the mixture was stirred for 5 h. Next, a solution containing 0.5 g of zinc phthalocyanine dissolved in 92.6 mL of tert-butyl alcohol and 36 mL of water was added. The system was stirred for 24 h, and the final sample was dried at 60 °C for 12 h.

2.2. Samples Characterization

Scanning electron microscopy (SEM) was used to observe the morphology and surface texture using a field-emission scanning electron microscope (Schottky JSM-7800F). Samples were imaged using a secondary electron detector at an acceleration voltage of 2.0 kV under ultra-high vacuum. Dimensions were measured using ImageJ software. High-resolution transmission electron microscopy (HR-TEM) was performed with a JEM-2100 microscope (LaB6 filament, 80–200 kV). Samples were suspended in isopropanol, sonicated to disperse, and deposited on a copper grid for analysis. X-ray diffraction (XRD) patterns were recorded using a Brucker D2 phaser diffractometer. The sample holder was filled with the corresponding sample to form a uniform surface and later introduced to the diffractometer, which uses Cu K α radiation ($\lambda = 1.5405$ nm), and a rate analysis of 0.0405°/sec in a 2 θ range from 7° to 80°. Raman spectroscopy was conducted at room temperature using a Jobin Yvon HR800 micro-Raman spectrometer. A 532 nm excitation laser with a D3 filter was used, and spectra were recorded from 0 to 3500 cm⁻¹ with a 2-second exposure time. Sample powders were placed in clean glass holders. Diffuse reflectance UV-Vis spectra were collected using a Varian Cary 100 Scan spectrophotometer equipped with a calcium sulfate integrating sphere, in the 190–800 nm range. Thermogravimetric analysis (TGA) was performed using a SAT-i 1000 instrument. Samples were heated from room temperature to 800 °C at 10 °C/min under nitrogen flow to determine weight loss. Nitrogen adsorption-desorption measurements were performed using Belsorp-mini II equipment. Samples were first degassed under vacuum at 60 °C for 12 h. Surface area, pore size, and pore volume were calculated from the isotherms.

2.3. *In Vitro* ROS Determination

1,3-diphenylisobenzofuran (DPBF) was used as a fluorescence uptake test for singlet oxygen formation. In brief: 200 mL a solution of BFS of 40 ppm of concentration was placed in a photoreactor (handmade) equipped with water recirculatory and air flux. Then the solution was bubbled with air for 20 min. After that, the 200 mg TiO₂ system was added and left in contact with the solution for 5 min. Subsequently, the solution was ir-radiated with an UV lamp of 2.2 mW, and 254 nm (from the UVP company). Each 2 min aliquots were removed from the solution for their measurement by UV-VIS spectroscopy through a Cary100SCAN UV-Vis spectrophotometer.

2.4. Biological Assays

Cell culture substances: Tetrazolium bromide (MTT) (Sigma-Aldrich, ≥97%), Fetal bovine serum (FBS) (Biowest), Dulbecco's Modified Eagle's Medium (DMEM) (Gibco), trypsin-EDTA (Gibco), antibiotic-antimycotic (Corning).

Cell line: LN18 and U251 (human glioblastoma cells) both were acquired by the ATCC company.

2.4.1. Cytotoxic Evaluation

To evaluate the cytotoxicity of the different TiO₂ systems developed, a cell viability assay was performed using the MTT (3-(4,5-dimethylthiazol-2-yl)-2,5-diphenyltetrazolium bromide) method on the human glioblastoma cell line LN18 and U251.

Cells were seeded at a density of 1×10^5 cells/well in 96-well plates and incubated overnight at 37 °C in a humidified atmosphere with 5% CO₂. The next day, cells were treated with increasing concentrations (0, 10, 25, 50, 100, and 500 µg/mL) of TiO₂, TiO₂-FA, and TiO₂-FA-ZnPc in DMEM with 5% FBS. Both treated and untreated cells were incubated for 24 h. MTT reagent was then added to each well and incubated for 2 h to allow formazan crystals to form in metabolically active cells. Next, 100 µL of acidified isopropanol (0.04 M HCl) was added to solubilize the crystals. Absorbance was measured at 570 and 630 nm using a microplate reader.

Cell viability was calculated using the following formula:

$$CV\% = (S(A570-A630))/(C(A570-A630)) \times 100\%$$

Where:

CV is the cell viability, S is the sample, C represents the control cells, A is the absorbance.

Experiments were performed in triplicate and included control groups of untreated cells. Results were expressed as percentages relative to the negative control. Statistical analysis was conducted using two-way ANOVA with Dunnett's post hoc test in GraphPad Prism (version 9.4.1).

2.4.2. Determination of the Phototoxicity Effect

To evaluate phototoxicity, differentiating treatment toxicity from light-dependent cytotoxicity. LN18 and U251 cells were seeded at 1×10^5 cells/well in 96-well plates and incubated overnight at 37 °C in a humid atmosphere with 5% CO₂ to allow adhesion. The next day, glioma cells were treated with increasing NPs concentrations (0, 10, 25, 50, 100, 250, and 500 µg/mL) of each dissolved in DMEM medium supplemented with FBS. After 10 minutes of treatment, cells were irradiated with exposed to 385 nm LED light for 1 or 10 min at distances of 1 and 10 cm. Irradiation was performed inside a laminar flow hood to prevent contamination and ensure consistent conditions.

Cells were then incubated for 24 h at 37 °C with 5% CO₂. Then, cell viability was assessed using an MTT colorimetric assay. For this, MTT was added to each well and incubated for 2 h. Then, the formed formazan crystals were solubilized with an isopropanol solution acidified with 0.04 M HCl. Absorbance was measured at 570 and 630 nm using a microplate reader. All treatments were done in triplicate. Results were expressed as percentage viability vs. untreated control. Data were analyzed using two-way ANOVA with Dunnett's test and paired Student's t-test for point comparisons. Data was analyzed using GraphPad Prism software (version 9.4.1).

3. Results

3.1. Characterization Results

SEM images were obtained using various magnifications while analyzing the different TiO₂ samples, as shown in Figure 1. The images corresponding to the TiO₂ sample reveal a morphology consisting of agglomerates of small particles ranging in size from approximately 10 to 100 nm (Figures 1a and b). These agglomerates form a porous network of TiO₂. Similarly, the TiO₂-FA sample exhibits a morphology made up of aggregated particles (Figure 1c and d). Likewise, the TiO₂-FA-ZnPc sample presents the same characteristics (Figure 1e and f). These nanoparticle aggregates yield a porous morphology in all samples, a characteristic typical of TiO₂ materials synthesized via the sol-gel method.

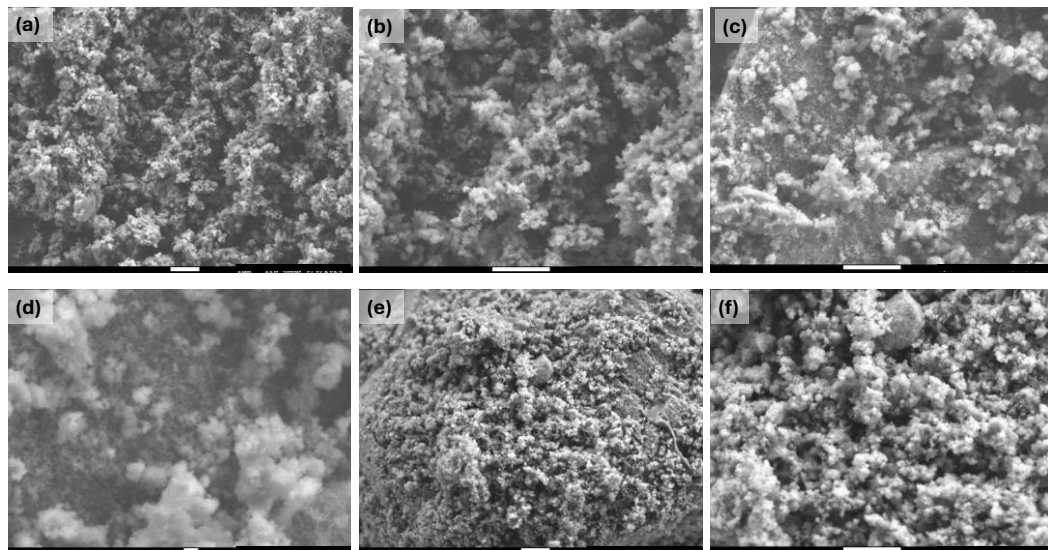


Figure 1. SEM images at different magnifications of the different prepared TiO₂ materials: (a) TiO₂ (x10,000), (b) TiO₂ (x20,000), (c) TiO₂-FA (x20,000), (d) TiO₂-FA (x50,000), (e) TiO₂-FA-ZnPc (x10,000), and (e) TiO₂-FA-ZnPc (x20,000). The scale bar in the (d) sample corresponds to 100 nm; the rest corresponds to 1 µm.

Figure 2 reports the high-resolution TEM (HR-TEM) images of the different TiO₂ materials prepared to be used as photosensitizers. The figures corresponding to the TiO₂ sample observed a mixture of amorphous and crystalline phases (Figure 2 (a) and (b)). In this case, the crystalline may be due to the formation of the anatase phase. In the sample functionalized with folic acid, greater crystallinity is observed, indicating that folic acid promotes the formation of the anatase phase (Figure 2 (b) and (c)). When ZnPc was added, distinct crystalline arrangements were observed.

Additionally, the presence of amorphous regions is evident in all samples. The HR-TEM images were also used to determine the interplanar spacing of the prepared TiO_2 -FA, and TiO_2 -FA-ZnPc materials. The interplanar spacing was calculated to be approximately 0.35 nm for the TiO_2 -AF sample. This crystallographic spacing is consistent with the (101) plane of anatase, as shown in Figure 1 (a). In Figure 1 (e), corresponding to TiO_2 -FA-ZnPc, a crystalline region is observed that is distinct from the rest of the sample. The lattice spacing calculated in this region is 0.47 nm, which can be attributed to the (202) plane of ZnPc and aligns well with values reported in the literature [34].

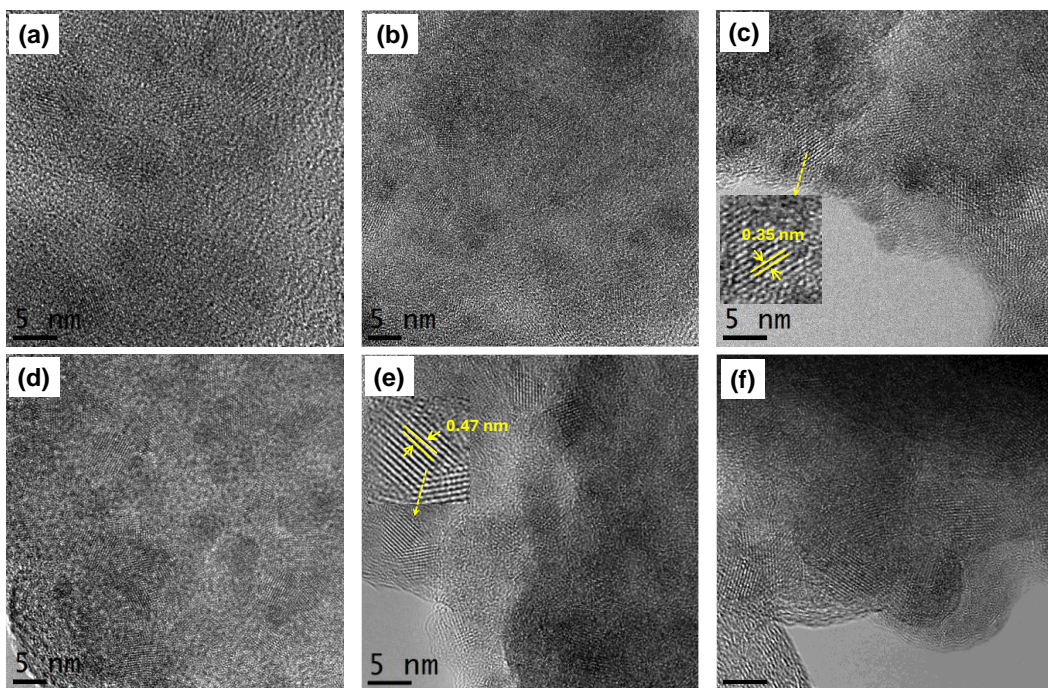


Figure 2. HR-TEM images of (a)-(b) TiO_2 , (c)-(d) TiO_2 -FA, and (e)-(f) TiO_2 -ZnPc. Zoomed regions show the interplanar spacing of (c) anatase phase and (e) ZnPc, respectively.

X-ray diffraction patterns are shown in Figure 3. The diffraction pattern of TiO_2 reveals a mixture of amorphous and anatase phases, as evidenced by the peak at 25.2° , corresponding to the (101) planes of anatase. The ZnPc spectrum exhibits sharp peaks characteristic of crystalline materials. The most intense peak appears at $2\theta = 9.34^\circ$, along with medium-intensity peaks at $2\theta = 7.08^\circ$ and 11.28° , and several minor peaks at $2\theta = 12.66^\circ$, 18.28° , 18.78° , 20.26° , 20.91° , 23.74° , and 26.29° , corresponding to different diffraction planes in ZnPc [34, 35]. In the diffractogram of the TiO_2 -FA-ZnPc sample, the features of TiO_2 dominate. However, the peak at $2\theta = 9.34^\circ$ corresponding to ZnPc is still visible, suggesting that ZnPc is integrated into the TiO_2 network. The XRD pattern of TiO_2 -FA closely resembles that of TiO_2 , indicating that folate is well dispersed within the porous titania structure.

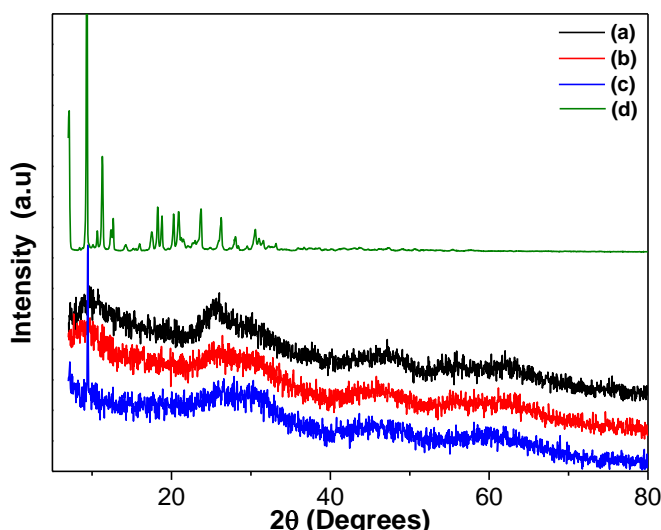


Figure 3. XRD patterns of the different TiO_2 materials: (a) TiO_2 , (b) $\text{TiO}_2\text{-FA}$, (c) $\text{TiO}_2\text{-FA-ZnPc}$, and (d) ZnPc .

Figure 4 shows the Raman spectra of the TiO_2 , $\text{TiO}_2\text{-FA}$, and $\text{TiO}_2\text{-FA-ZnPc}$ samples in the 0–3500 cm^{-1} range. Figure 4 (a) displays an intense and well-defined peak at 150 cm^{-1} , associated with the anatase crystalline phase of TiO_2 ($\text{Eg}(2)$ mode). The signal at 623 cm^{-1} is also attributed to the anatase phase due to the Eg vibration mode, while the peak at 404 cm^{-1} corresponds to the B1g mode of anatase [36]. The Raman spectrum of $\text{TiO}_2\text{-FA}$ closely resembles that of TiO_2 , with only a slight shift in the band at 637 cm^{-1} due to the presence of folic acid (Figure 4b), suggesting that folic acid is well dispersed within the TiO_2 network. In $\text{TiO}_2\text{-FA-ZnPc}$ (Figure 4c), in addition to the TiO_2 -related signals, other well-defined peaks are predominant throughout the spectrum. According to literature reports, the peak at 588 cm^{-1} originates from benzene ring deformation; the peak at 675 cm^{-1} is associated with the macrocycle, and the peaks at 1344 cm^{-1} and 1513 cm^{-1} are attributed to the Zn metal ion linked to the phthalocyanine molecule [37, 38]. In the 2000–3800 cm^{-1} region, carbon-related vibrations from ZnPc are also observed.

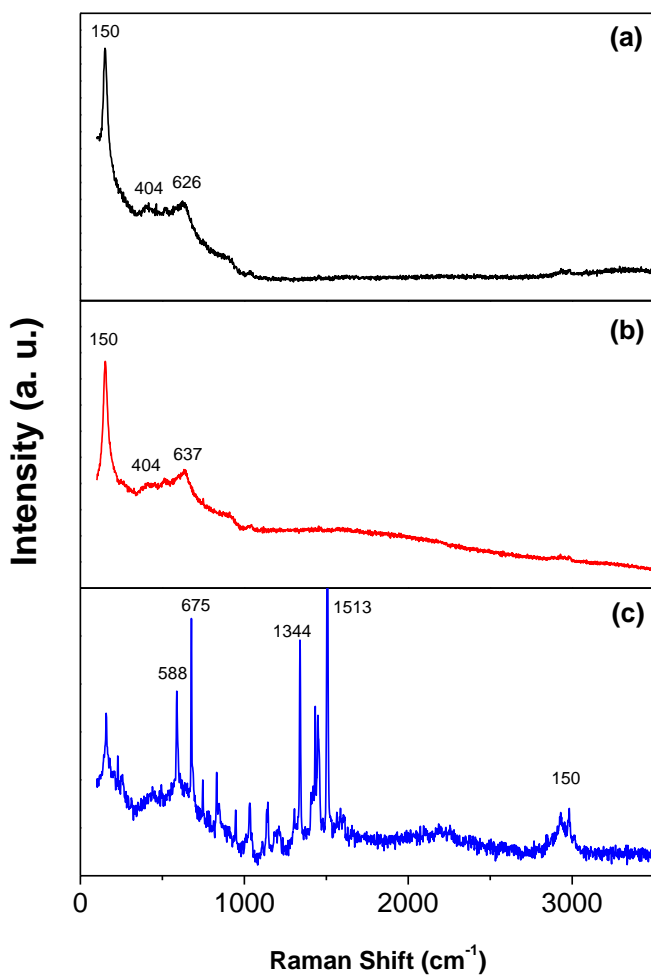


Figure 4. Raman spectra of the (a) TiO_2 , (b) TiO_2 -FA, and (c) TiO_2 -FA-ZnPc materials.

The UV-Vis diffuse reflectance spectra in the solid state of TiO_2 , TiO_2 -FA, and TiO_2 -FA-ZnPc materials are shown in Figure 5. The TiO_2 spectrum displays a strong absorption band at 380 nm (Figure 5a), which corresponds to an electron transition from the 3d orbital of the titanium atom to the 2p orbitals of the oxygen atoms in TiO_2 [39]. The TiO_2 -FA spectrum closely resembles that of TiO_2 ; however, the strong absorption peak is red-shifted from 380 nm to 520 nm. This shift can be attributed to interactions between the folic acid molecules and the TiO_2 surface. The ZnPc spectrum exhibits multiple absorption signals across the UV-Vis range, which can be divided into visible and ultraviolet regions. In the visible region, signals between 450 and 750 nm correspond to the Q-band ($\lambda = 660 \text{ nm}$), while the UV region features the B-band ($\lambda = 327 \text{ nm}$) [40]. The Q-band is attributed to p-p* transitions from the highest occupied molecular orbital (HOMO) to the lowest unoccupied molecular orbital (LUMO) in ZnPc. The B-band arises from transitions from deeper p levels to the LUMO [41]. In the TiO_2 -FA-ZnPc spectrum, the Q-band of ZnPc is observed in the visible region, as shown in the magnified view in Figure 5B. The ultraviolet band is not visible, possibly due to overlap with the TiO_2 absorption band. The bandgap energy (E_g) calculated from experimental data for TiO_2 was 3.46 eV. In contrast, the E_g values for TiO_2 -FA and TiO_2 -FA-ZnPc were 2.38 eV. Notably, visible region signals were observed in the TiO_2 -FA-ZnPc spectrum.

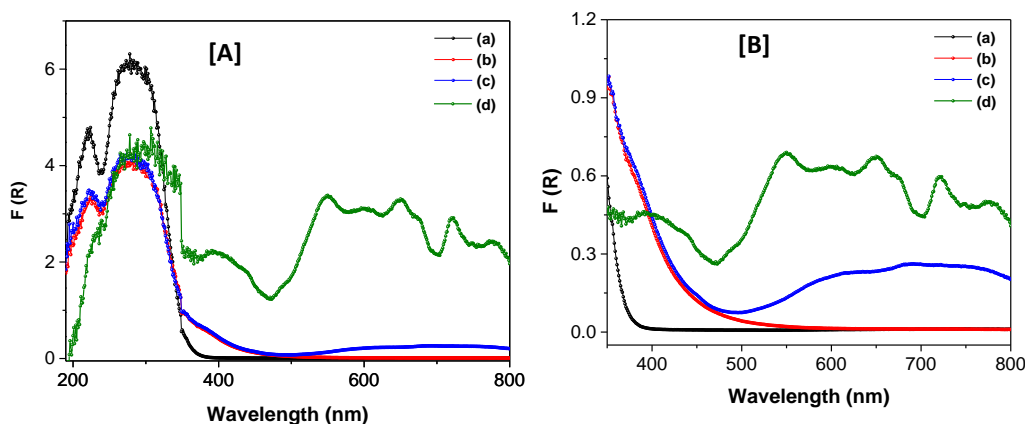


Figure 5. UV-Vis spectra of the different based TiO_2 materials in their solid state [A] in the 200-800 range and [B] in the 350-800 range, respectively. (a) TiO_2 , (b), TiO_2 -FA, (c) TiO_2 -FA-ZnPc, and (d) ZnPc.

Figure 6 displays the nitrogen adsorption-desorption isotherms of the various synthesized TiO_2 materials. According to the IUPAC classification, all isotherms correspond to Type IV, which is typical of mesoporous materials. A hysteresis loop, classified by IUPAC as H1, is also observed, confirming the mesoporous nature of the materials. At low P/P_0 values, an adsorbed volume between 0.01-0.2 nm is detected, indicative of micropores not captured in N_2 analysis, as shown in the pore size distribution (inset in Figure 6). Additional adsorption at higher P/P_0 values (0.95–1.0) suggests the presence of macropores, although in smaller amounts compared to micro- and mesopores. Overall, both micro- and macropores are present in lesser quantities than mesopores.

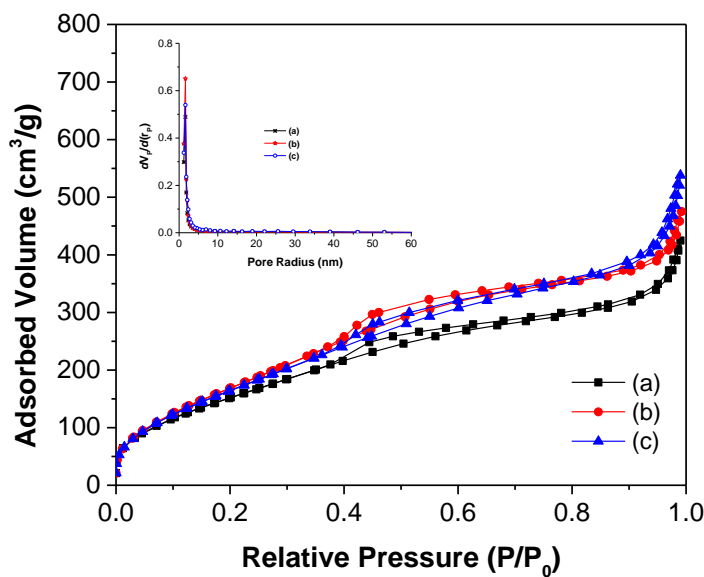


Figure 6. N_2 adsorption-desorption isotherms of (a) TiO_2 , (b) TiO_2 -FA, and (c) TiO_2 -FA-ZnPc materials. The insert shows the pore size distribution of the materials.

Textural properties such as surface area, average pore diameter, and pore volume were derived from the nitrogen adsorption-desorption isotherms and are summarized in Table 1. The surface area for TiO_2 was 602 nm, while those for TiO_2 -FA and TiO_2 -FA-ZnPc were 706 and 675 nm, respectively. All values are relatively high. Notably, the surface area increased upon the addition of folic acid. However, when ZnPc was incorporated, the surface area decreased by 4.31% compared to the TiO_2 -FA sample. This reduction may be due to ZnPc molecules occupying part of the pores and surface, as they were added after the TiO_2 -FA network had formed. The average pore diameter decreased from 5.35 nm in TiO_2 to 4.07 nm in TiO_2 -FA, likely due to folic acid molecules occupying the pore

spaces. The pore volume followed the trend: $\text{TiO}_2\text{-FA-ZnPc} > \text{TiO}_2\text{-FA} > \text{TiO}_2$, with all materials exhibiting relatively high pore volumes.

Table 1. Textural and bandgap values of the different TiO_2 , $\text{TiO}_2\text{-AF}$, and $\text{TiO}_2\text{-AF-ZnPc}$ materials. S_{BET} is surface area, P_D is the pore diameter, and P_V is the pore volume.

Sample	S_{BET}^* (m^2/g)	P_D^{**} (nm)	P_V^{**} (cc/g)	Bandgap (eV)
TiO_2	602	5.35	0.6564	3.46
$\text{TiO}_2\text{-AF}$	706	4.07	0.7199	2.38
$\text{TiO}_2\text{-AF-ZnPc}$	675	4.90	0.8289	2.38

*Obtained by the adsorption isotherm and using the BETH method, ** obtained from the desorption isotherm and using the BJH method.

The weight loss profiles as a function of treatment temperature for the TiO_2 , $\text{TiO}_2\text{-FA}$, and $\text{TiO}_2\text{-FA-ZnPc}$ samples are shown in Figure 7, with corresponding percentage weight loss values for each temperature range presented in Table 2. The thermogram for TiO_2 shows two significant weight loss events: the first occurs between room temperature and 150 °C and corresponds to the evaporation of volatile compounds such as water and alcohol used during synthesis, accounting for a 14% loss (Table 2). The second weight loss occurs between 150–300 °C, likely due to residual precursor materials such as alkoxides, resulting in an 8% loss. Beyond this temperature range, the thermogram becomes linear, indicating no further weight loss. The thermogram for $\text{TiO}_2\text{-FA}$ displays three distinct stages of weight loss. The first stage, between room temperature and 150 °C, also corresponds to the loss of water and alcohol, accounting for 14%. The second stage, from 150–300 °C, shows an 8% weight loss related to the elimination of organic precursors. The third stage, from 300–426 °C, exhibits a 3% weight loss, attributed to the complete degradation of folic acid. After this, a stable, linear profile indicates no additional weight loss. In total, 20 g of TiO_2 were synthesized, to which 0.5 g of folic acid was added, representing 2.5% of the TiO_2 mass. The observed 3% weight loss attributed to folic acid (Table 2) closely aligns with the theoretical value, confirming through TGA the composition of the sample. The thermogram for the $\text{TiO}_2\text{-FA-ZnPc}$ sample reveals four main weight loss stages. As in the previous sample, the first three stages correspond to (1) the loss of water and alcohol and (2-3) the removal of folic acid, with similar percentage losses to $\text{TiO}_2\text{-FA}$ (Table 2). The fourth stage, occurring between 426–600 °C, reflects the degradation of ZnPc, showing a 2% weight loss. This value is also consistent with the 2.5% ZnPc added during synthesis, further confirming the composition of the sample.

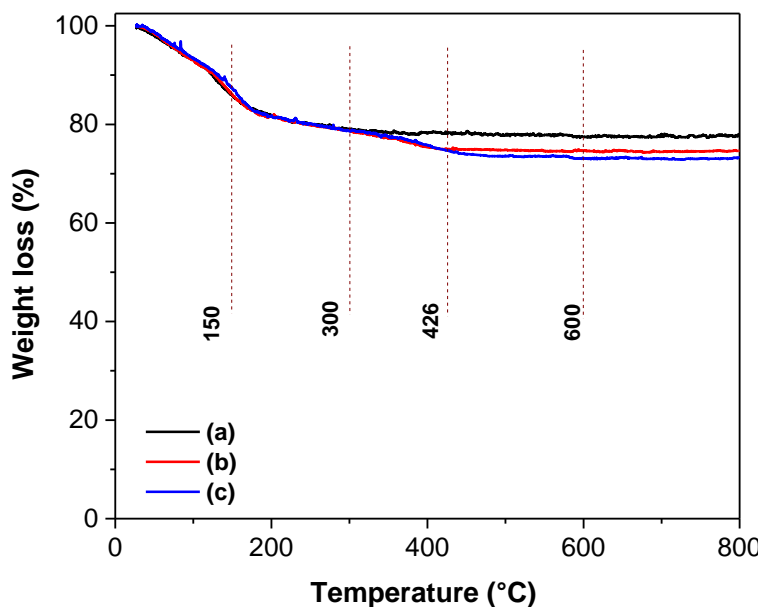


Figure 7. TGA curves of the different TiO_2 -based materials: (a) TiO_2 , (b) $\text{TiO}_2\text{-FA}$, and (c) $\text{TiO}_2\text{-FA-ZnPc}$.

Table 2. weight loss % at different temperature intervals of the TiO_2 , $\text{TiO}_2\text{-FA}$, and $\text{TiO}_2\text{-FA-ZnPc}$ samples.

Sample	Weight loss (%)			
	25-150 °C	150-300 °C	300-426 °C	426-600 °C
TiO_2	14	8		
$\text{TiO}_2\text{-AF}$	14	8	3	
$\text{TiO}_2\text{-FA-ZnPc}$	13	9	3	2

3.2. In Vitro ROS Production

The generation of singlet oxygen was confirmed using 1,3-diphenylisobenzofuran (DPBF) as a probe. Figure 8 shows the UV-Vis absorption spectra of DPBF in the presence of TiO_2 , $\text{TiO}_2\text{-FA}$, and $\text{TiO}_2\text{-FA-ZnPc}$ after UV light irradiation for up to 16 min. The absorption intensity of DPBF gradually decreases over time, as the solution transitions from green to colorless. Complete degradation of DPBF was observed after 10 min of irradiation with TiO_2 , 12 min with $\text{TiO}_2\text{-FA}$, and 14 min with $\text{TiO}_2\text{-FA-ZnPc}$.

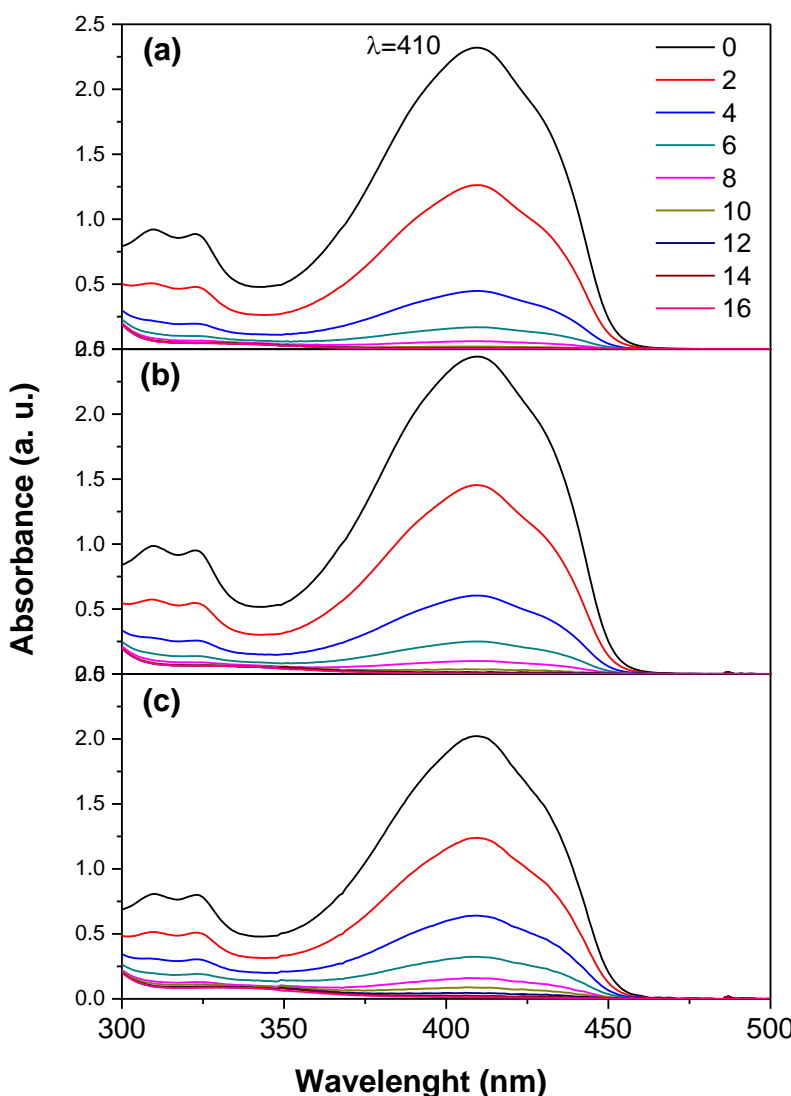


Figure 9. UV-Vis spectra of the 1,3-diphenylisobenzofuran (DPBF) in the presence of the TiO_2 samples after irradiation with UV light for different times (0-16 min). (a) TiO_2 , (b) $\text{TiO}_2\text{-FA}$, (c) $\text{TiO}_2\text{-FA-ZnPc}$.

3.3. Biological Results

The viability of LN18 and U251 cells was evaluated using the MTT assay after 24 h of exposure to TiO_2 , $\text{TiO}_2\text{-FA}$, and $\text{TiO}_2\text{-FA-ZnPc}$ materials (Figure 9). This assay quantifies cell metabolic activity,

which serves as an indicator of cytotoxicity. The results show that the average viability of LN18 cells exposed to various concentrations of the TiO_2 -based materials (5-100 $\mu\text{g}/\text{mL}$) decreased by increasing TiO_2 concentration in a dose-dependent manner over time. After 24 h, cell viability remained high at low and moderate concentrations ($\leq 100 \mu\text{g}/\text{mL}$) for all three systems, suggesting good initial biocompatibility (Figure 9a). However, at concentrations of 250 $\mu\text{g}/\text{mL}$ and above, significant cytotoxic effects were evident.

At the lowest concentrations (10-100 $\mu\text{g}/\text{mL}$), cell viability remained relatively high, with no significant differences from the control group. However, at concentrations between 250 and 500 $\mu\text{g}/\text{mL}$, a statistically significant decrease in viability was recorded, particularly for the TiO_2 -FA-ZnPc group, where notable differences began to appear at 250 $\mu\text{g}/\text{mL}$ ($p < 0.05$), according to Dunnett's analysis.

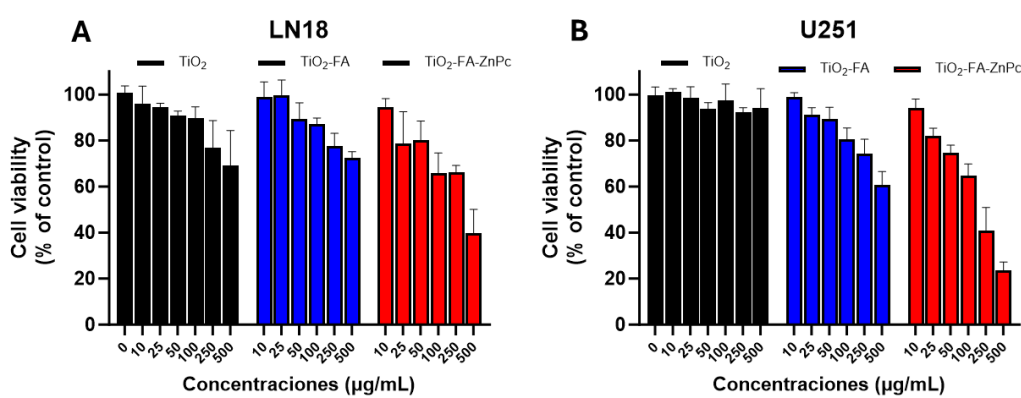


Figure 9. Viability of LN18 and U251 cells after treatment with different concentrations of TiO_2 (black), TiO_2 -FA (blue), and TiO_2 -FA-ZnPc (red) nanoparticles (24h). The standard deviations are indicated with the error bars.

As shown in Figure 10 and 11, the cell viability TiO_2 -ZnPc nanoparticles combined with UV irradiation enhance cell death from 100 $\mu\text{g}/\text{mL}$ in all conditions although the LN18 cells shower been more resistant than U251 cells. These last cells responded in a doses light dependent differential effect at 10 cm and increase time.

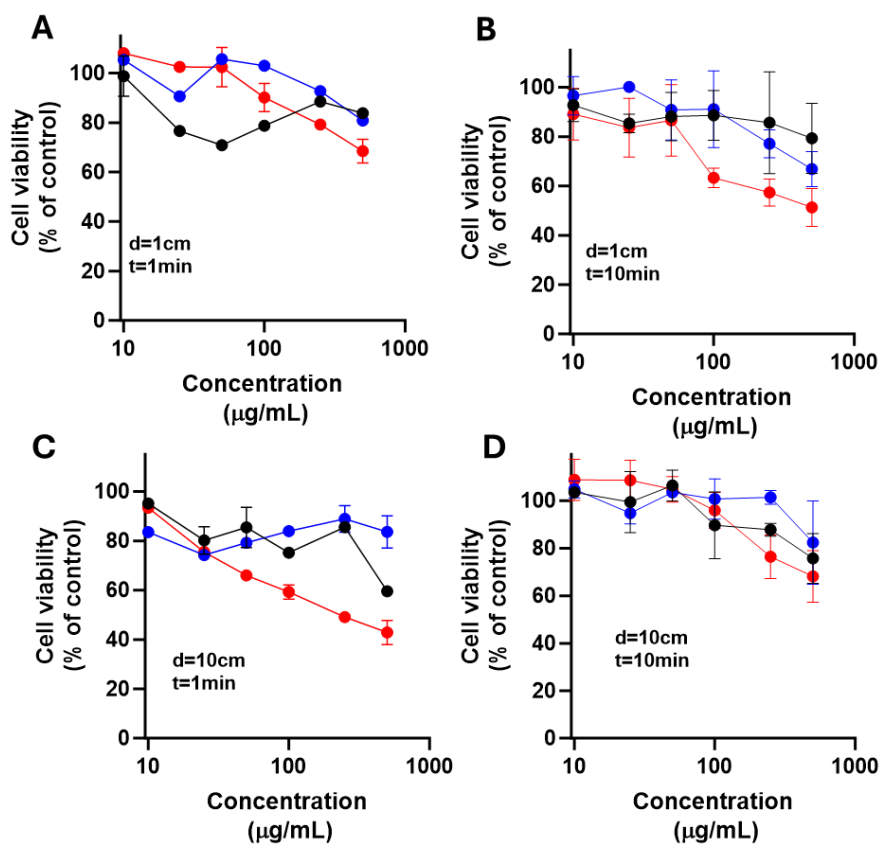


Figure 10. Effect of nanoparticles over cell viability after irradiation on LN18 cells.

The cells were exposed to LED light at 385nm for 1min (A and C) or 10min (B and D) with 1cm (A and B), and 10cm (C and D) of irradiation source, after 24h cell viability was determined. Results are expressed as means \pm SEM.

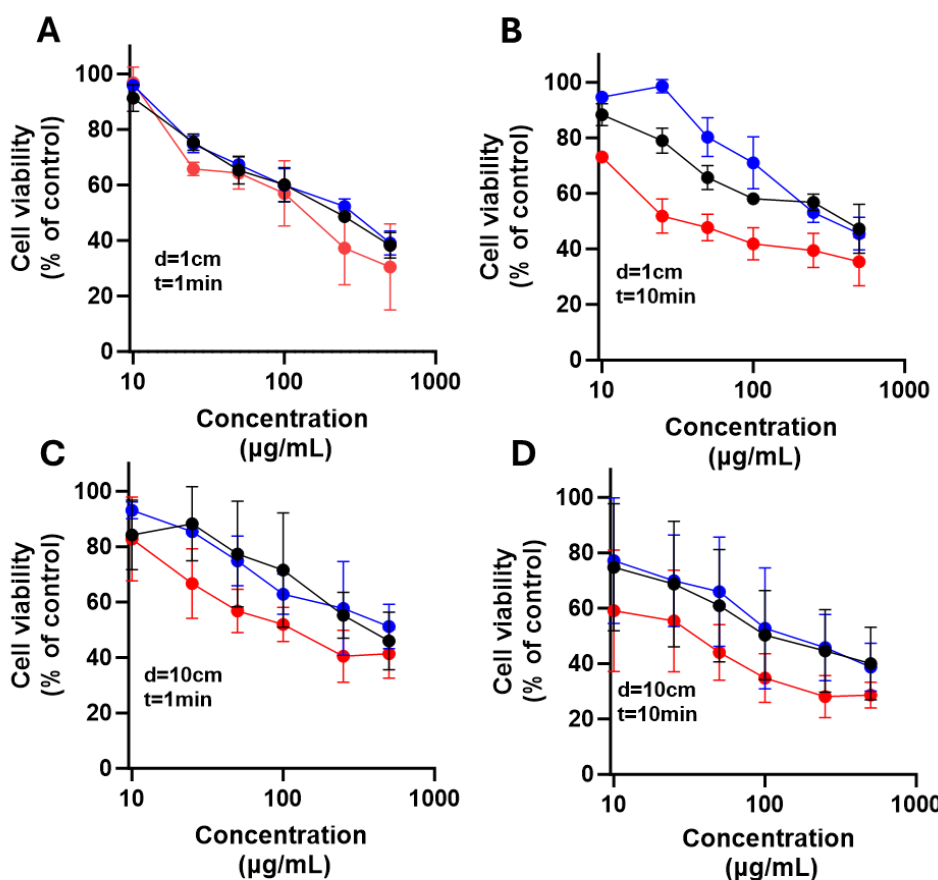


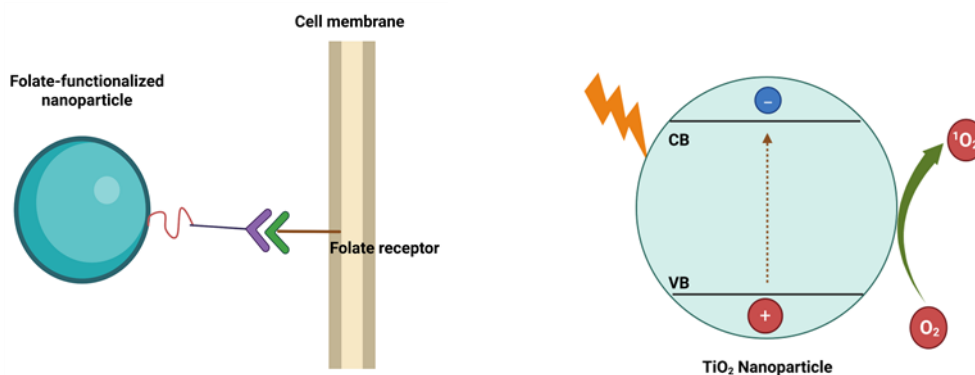
Figure 11. Effect of nanoparticles over cell viability after irradiation on U251 cells. The cells were exposed to LED light at 385nm for 1min (A and C) or 10min (B and D) with 1cm (A and B), and 10cm (C and D) of irradiation source, after 24 h cell viability was determined. Results are expressed as means \pm SEM.

4. Discussion

Folic acid, also known as vitamin B9, is a water-soluble vitamin essential for the synthesis of nitrogenous bases in nucleotide formation within cells [42]. Cancer cells require increased amounts of folate for their proliferation and survival. Consequently, folic acid plays a critical role in supporting the growth of cancer cells, which often overexpress folate receptors to enhance folate uptake. For this reason, folic acid is commonly used to functionalize the surfaces of nanomaterials, enabling selective targeting of cancer cells [43]. Folate-functionalized nanomaterials can enter cancer cells via folate receptor-mediated endocytosis (Scheme 2 (a)). This targeted approach is feasible because most healthy tissues exhibit low expression of folate receptors, allowing discrimination between cancerous and normal cells. Therefore, the TiO_2 -FA system was designed to provide selective interaction with glioma cells through folate receptor engagement.

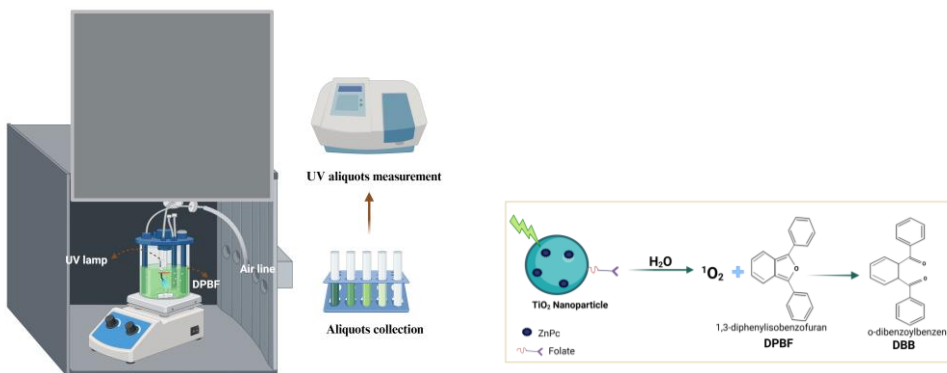
Initially, only TiO_2 nanoparticles were synthesized, exhibiting desirable physicochemical characteristics including a nanostructured morphology, high surface area ($602 \text{ m}^2/\text{g}$), mesoporous structure (average pore size of 5.35 nm), a mixed anatase-amorphous phase, and a bandgap of 3.46 eV , a typical value for semiconductor TiO_2 . These properties allowed for the uniform incorporation and dispersion of folic acid throughout the TiO_2 network, yielding a composite material with distinct characteristics: a larger surface area of $706 \text{ m}^2/\text{g}$ while preserving the mesoporous structure (4.07 nm pore size) and mixed-phase composition. This was achieved via the sol-gel method, a process widely used to introduce active species homogeneously and in-situ, eliminating the need for post-synthesis modifications [44]. Thermogravimetric analysis confirmed that the incorporated amounts of folic acid and ZnPc closely matched their theoretical values (Table 2). A photosensitizing nanocomposite was subsequently obtained by loading ZnPc onto the TiO_2 -FA structure. This final material retained its unique features while also enhancing the functional

properties of both TiO_2 and ZnPc. The TiO_2 -FA-ZnPc composite had a high surface area of $675 \text{ m}^2/\text{g}$ and exhibited strong absorption bands in both UV and visible regions, resulting in a reduced bandgap of 2.3 eV.



Scheme 2. This is a schematic representation of the functionalization of a TiO_2 nanoparticle with folic acid and its subsequent entry into a cell via folate receptors. It also shows ROS formation when TiO_2 nanoparticles are irradiated with UV light.

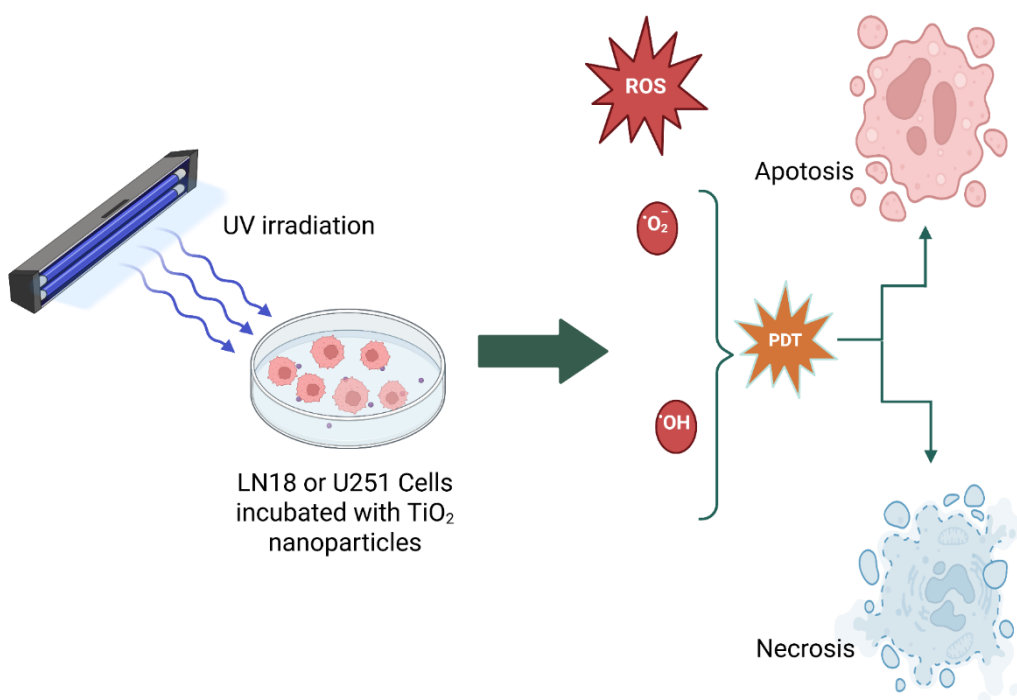
Titania is a well-known semiconductor that generates significant amounts of reactive oxygen species (ROS) under UV irradiation (Scheme 2). An in-situ study was performed using the DPBF probe to evaluate ROS generation by TiO_2 . DPBF (Scheme 3) is a widely used fluorescent probe for ROS detection, as it undergoes oxidative bleaching to form the colorless compound 1,2-dibenzoylbenzene (DBB) (Scheme 3) [45]. DPBF exhibits a characteristic absorption band at approximately 415 nm, which disappears when singlet oxygen ($^1\text{O}_2$) reacts rapidly with the probe (Figure 8). The ROS generation results indicate that TiO_2 degrades DPBF more rapidly than TiO_2 -FA and TiO_2 -FA-ZnPc. However, functionalization with folic acid is essential for obtaining a TiO_2 -based material that targets specific cells. On the other hand, ZnPc tends to aggregate in solution and thus requires stabilization by a high surface area support material that can also be functionalized to effectively disperse ZnPc and facilitate ROS production.



Scheme 3. This is a schematic representation of the photocatalytic test using DPBF. This is the proposed reaction mechanism between the produced singlet oxygen and DPBF.

LN-18 and U-251 MG human glioblastoma multiforme (GBM) cell that is extensively used in neuro-oncology research. LN-18 cells line was originally isolated in 1976 from the right temporal lobe of a 65-year-old White male patient diagnosed with glioblastoma [46]. While U-251 MG cell line was derived originally from a 75-year-old Caucasian male. In this study, these two cell lines were employed to evaluate the cytotoxicity of the synthesized TiO_2 -based materials. Cell viability assays using the MTT method showed that the materials retained acceptable biocompatibility at low and moderate concentrations. Specifically, viability remained above 80% during the first 24 h of exposure at concentrations up to $100 \mu\text{g}/\text{mL}$, indicating that the LN18 and U251 cells tolerated the materials well under physiological conditions and in the absence of irradiation.

Scheme 4 is a schematic representation showing that, when cancer cells combined with different TiO_2 nanoparticle systems and irradiated with UV light, the produced ROS and cause cell death mainly by apoptosis, necrosis and/or autophagy.



Scheme 4. A schematic representation of photodynamic therapy, which is used to kill glioma cells (LN18 or U251 cells).

5. Conclusions

Using the sol-gel method, TiO_2 nanoparticles were synthesized with desirable physicochemical properties, including a large surface area, a mesoporous structure, and a mixed amorphous-anatase phase. These nanoparticles also exhibited the characteristic bandgap energy of TiO_2 at 3.46 eV. These features were preserved following functionalization with folic acid. Additionally, by incorporating ZnPc into the TiO_2 -FA structure, a multifunctional nanocomposite was obtained that combined the properties of both folic acid and ZnPc. These materials exhibited enhanced ROS generation, as demonstrated by the rapid degradation of DPBF to the non-colored compound DBB. The nanomaterials were shown to be non-toxic at low concentrations; however, at higher doses, a reduction in cell viability was observed. The photoactivity assays indicated that cell death was dependent on both the concentration of the nanomaterial and the duration of UV light exposure. Importantly, the presence of the nanomaterials alone did not harm LN18 cells when compared to cells exposed to UV light without nanoparticles.

Author Contributions: Conceptualization, E.O.I.; methodology, E.O.I., S.R.G., M.E.M.R., A.M.O.T., F.T. and C.E.R.P.; formal analysis, E.O.I., S.R.G., M.E.M.R., A.M.O.T., F.T. and C.E.R.P.; investigation, E.O.I. resources, E.O.I.; data curation, E.O.I., M.E.M.R. and C.E.R.P.; writing—original draft preparation, E.O.I.; writing—review and editing, E.O.I.; supervision, E.O.I., M.E.M.R., F.T. and E.E.R.P.; project administration, E.O.I.; funding acquisition, E.O.I. All authors have read and agreed to the published version of the manuscript.

Funding: This research was funded by Secretaría de Ciencia, Humanidades, Tecnología e Innovación (SECIHTI), México, grant number CBF2023-2024-1982.

Institutional Review Board Statement: Not applicable.

Informed Consent Statement: Not applicable.

Data Availability Statement: Dataset available on request from the authors.

Acknowledgments: S.R.G. acknowledges the SECIHTI-Mexico Master Fellowship (1349443).

Conflicts of Interest: The authors declare no conflicts of interest.

Abbreviations

The following abbreviations are used in this manuscript:

TiO ₂	Titanium dioxide
ROS	Reactive Oxygen Species
PDT	Photodynamic Therapy
DNA	Deoxyribonucleic acid
UV	Ultraviolet
PS	Photosensitizer
PSES	Photosensitizer excited state
PSET	Photosensitizer excited triplet
WHO	World Health Organization
TMZ	Temozolomide
BBB	Blood Brain Barrier
ZnPc	Zin Phthalocyanine
FA	Folic Acid
DPBF	1,3-Diphenylisobenzofuran
SEM	Scanning Electron Microscopy
HR-TEM	High Resolution transmission Electron Microscopy
XRD	X ray diffraction
TGA	Thermogravimetric Analysis
VIS	Visible
MTT	Tetrazolium Bromide
FBS	Fetal Bovine Serum
DMEN	Dulbecco's Modified Eagle's
HOMO	Highest Occupied Molecular Orbital
LUMO	Less Unoccupied Molecular Orbital
Eg	Bandgap Energy
BET	Brunauer-Emmett-Teller method
BJH	Barrett-Joyner-Halenda method

References

1. Racovita, A.D. Titanium dioxide: Structure, impact, and toxicity. *Int. J. Environ. Res. Public Health.* **2022**, *19*, 1-20.
2. Lugo-Ruiz, A.A.; Paz-Ruiz, M.J.; Bailón-Ruiz, S.J. Photodegradation of organic dyes in single and multi-component in the presence of titanium dioxide nanoparticles. *MRS Adv.* **2022**, *7*, 255-259.
3. Park, Y.K.; Kim, B.J.; Jeong, S.; Jeon, K.J.; Chung, K.H.; Jung, S.C. Characteristics of hydrogen production by photocatalytic water splitting using liquid phase plasma over Ag-doped TiO₂ photocatalysts. *Environ. Res.* **2020**, *188*, 1-8.
4. Manríquez-Ramírez, M.E.; Reza San German, C.; Estrada Flores, M.; Trejo Valdez, M.; Ortiz-Islas, E. Styrene oxide hydrogenation reaction using Pt/TiO₂-ZrO₂ supported catalysts for 2-phenylethanol production. *Mater. Res. Bull.* **2020**, *128*, 1-10.
5. Morgunov, V.; Lytovchenko, S.; Chyshkala, V.; Riabchikov, D.; Matviienko, D. Comparison of anatase and rutile for photocatalytic applications: The short review. *East Eur. J. Phys.* **2021**, *4*, 18-30.
6. Grinberg, V.A.; Emets, V.V.; Tsodikov, M.V.; Mayorova, N.A.; Maslov D.A. Photoelectrocatalytic degradation of organic compounds on nanoscale semiconductor materials. *Prot. Met. Phys. Chem. Surf.* **2021**, *57*, 699-712.
7. Akhter, P.; Arshad, A.; Saleem, A.; Hussain, M. Recent development in non-metal-doped titanium dioxide photocatalysts for different dyes degradation and the study of their strategic factors: A review. *Catal.* **2022**, *12*, 1-32.
8. Tsoi, C.C.; Huang, X.W.; Leung, P.H.M.; Wang, N.; Yu, W.X.; Jia, Y.W.; Li, Z.H.; Zhang, X.M. Photocatalytic ozonation for sea water decontamination. *J. Water Process Eng.* **2020**, *37*, 1-8.

9. Silva, M.R.F.; Lourenço, M.A.O.; Tobaldi, D.M.; da Silva, C.F.; Seabra, M.P.; Ferreira, P. Carbon-modified titanium oxide materials for photocatalytic water and air decontamination. *Chem. Eng. J.* **2020**, *87*, 1-13.
10. Lingaraju, K.; Basavaraj, R.B.; Jayanna, K.; Bhavana, S.; Devaraja, S.; Kumar Swamy, H.M.; Nagaraju, G.; Nagabhushana, H.; Naika H.R. Biocompatible fabrication of TiO₂ nanoparticles: Antimicrobial, anticoagulant, antiplatelet, direct hemolytic and cytotoxicity properties. *Inorg. Chem. Commun.* **2021**, *127*, 1-9.
11. Pawar, T.J.; Contreras López, D.; Olivares Romero, J.L.; Vallejo Montesinos, J. Surface modification of titanium dioxide. *J. Mater. Sci.* **2023**, *58*, 6887-6930.
12. Öztürk, U.Ş.; Çitak, A. Synthesis of titanium dioxide nanoparticles with renewable resources and their applications: review. *Turk. J. Chem.* **2022**, *46*, 1345-1357.
13. Sargazi, S.; Simge, E.R.; Gelen, S.S.; Rahdar, A.; Bilal, M.; Arshad, R.; Ajalli, N.; Khan, M.F.A.; Pandey, S. Application of titanium dioxide nanoparticles in photothermal and photodynamic therapy of cancer: An update and comprehensive review. *J. Drug Deliv. Sci. Technol.* **2022**, *75*, 1-14.
14. Ramachandran, P.; Khor, B.K.; Lee, C.Y.; Doong, R.A.; Oon, C.E.; Thanh, N.T.K.; Lee, H.L. N-doped graphene quantum dots/titanium dioxide nanocomposites: A study of ROS-forming mechanisms, cytotoxicity and photodynamic therapy. *Biomedicines* **2022**, *10*, 1-19.
15. Hou, Y.K.; Mushtaq, A.; Tang, Z.; Dempsey, E.; Wu, Y.L.; Lu, Y.G.; Tian, C.; Farheen, J.; Kong, X.D.; Iqbal, M.Z. ROS-responsive Ag-TiO₂ hybrid nanorods for enhanced photodynamic therapy of breast cancer and antimicrobial applications. *J. Sci.: Adv. Mater. Devices* **2022**, *7*, 1-9.
16. Flak, D.; Coy, E.; Nowaczyk, G.; Yate, L.; Jurg, S. Tuning the photodynamic efficiency of TiO₂ nanotubes against HeLa cancer cells by Fe-doping. *RSC Adv.* **2015**, *5*, 85139-85152.
17. Fakhar-e-Alam, M.; Aqrab-ul-Ahmad; Atif, M.; Alimgeer, K.S.; Rana, M.S.; Yaqub, N.; Farooq, W.A.; Ahmad, H. Synergetic effect of TEMPO-coated TiO₂ nanorods for PDT applications in MCF-7 cell line model. *Saudi J. Biol. Sci.* **2020**, *27*, 3199-3207.
18. Lin, S.L.; Chen, H.C.; Chang, C.A. Enhancing Förster resonance energy transfer (FRET) efficiency of titania–lanthanide hybrid upconversion nanomaterials by shortening the donor–acceptor distance. *Nanomaterials* **2020**, *10*, 1-14.
19. Ziental, D.; Czarczynska-Goslinska, B.; Mlynarczyk, D.T.; Glowacka-Sobotta, A.; Stanisz, B.; Goslinski, T.; Sobotta, L. Titanium dioxide nanoparticles: Prospects and applications in medicine. *Nanomaterials* **2020**, *10*, 1-31.
20. Youssef, Z.; Vanderesse, R.; Colombeau, L.; Baros, F.; Roques-Carmes, T.; Frochot, C.; Wahab, H.; Toufaily, J.; Hamieh, T.; Acherar, S.; Gazzali, A.M. The application of titanium dioxide, zinc oxide, fullerene, and graphene nanoparticles in photodynamic therapy. *Cancer Nano* **2017**, *8*, 1-62.
21. Aebisher, D.; Szpar, J.; Bartusik-Aebisher, D. Advances in medicine: Photodynamic therapy. *Int. J. Mol. Sci.* **2024**, *25*, 1-22.
22. Aebisher, D.; Rogoz, K.; Mysliwiec, A.; Dynarowicz, K.; Wiench, R.; Cieslar, G. Kawczyk-Krupka, A.; Bartusik-Aebisher, D. The use of photodynamic therapy in medical practice. *Front. Oncol.* **2024**, *14*, 1-25.
23. Dong, C.; Yi, Q.; Fang, W.; Zhang, J. A mini review of nanomaterials on photodynamic therapy. *J. Photochem. Photobiol. C: Photochem. Rev.* **2023**, *54*, 1-11.
24. Li, H.X.; Shen, J.J.; Zheng, C.F.; Zhu, P.; Yang, H.; Huang, Y.X.; Mao, X.R.; Yang, Z.L.; Hu, G.D.; Chen, Y.H. Cell death: The underlying mechanisms of photodynamic therapy for skin diseases. *Interdiscip. Med.* **2024**, *3*, 1-24.
25. Kwiatkowski, S.; Knap, B.; Przystupski, D.; Saczko, J.; Kędziersk, E.; Knap-Czop, K.; Kotliński, J.; Michel, O.; Kotowski, K.; Kulbacka, J. Photodynamic therapy– mechanisms, photosensitizers and combinations. *Biomed. Pharmacother.* **2018**, *106*, 1098-1107.
26. Allison, R.R.; Sibata, C.H. Oncologic photodynamic therapy photosensitizers: A clinical review. *Photodiagnosis Photodyn. Ther.* **2010**, *7*, 61-75.
27. Mfouo-Tynga, I.S.; Dias, L.D.; Inada, N.M.; Kurachi, C. Features of third generation photosensitizers used in anticancer photodynamic therapy: Review. *Photodiagnosis Photodyn. Ther.* **2021**, *34*, 1-11.

28. Chen, J.M.; Fan, T.J.; Xie, Z.J.; Zeng, Q.Q.; Xue, P.; Zheng, T.T.; Chen, Y.; Luo, X.L.; Zhang, H. Advances in nanomaterials for photodynamic therapy applications: Status and challenges. *Biomater.* **2020**, *237*, 1-27.

29. Ma, S.H.; Jiang, L.X.; Yang, W.J.; Liu, F.; Wang, D.; Wang, F.; Huang, J. Advances of nanomaterials in cancer photocatalysis therapy. *Mater. Today Sustain.* **2025**, *29*, 1-17.

30. Liu, L.; Yang, M.; Chen, Z. Surface functionalized nanomaterial systems for targeted therapy of endocrine related tumors: A review of recent advancements. *Drug Deliv.* **2024**, *31*, 1-18.

31. Persano, L.; Rampazzo, E.; Basso, G.; Viola, G. Glioblastoma cancer stem cells: Role of the microenvironment and therapeutic targeting. *Biochem. Pharmacol.* **2013**, *85*, 612-622.

32. Johnson, D.R.; O'Neill, B.P. Glioblastoma survival in the United States before and during the temozolomide era. *J. Neurooncol.* **2012**, *107*, 359-364.

33. Adnane, F.; El-Zayat, E.; Fahmy, H.M. The combinational application of photodynamic therapy and nanotechnology in skin cancer treatment: A review. *Tissue Cell.* **2022**, *77*, 1-18.

34. Yoon, Y.; Kim, S.; Choi, H.C. Selective growth of α -form zinc phthalocyanine nanowire crystals via the flow rate control of physical vapor transport. *NPG Asia Mater.* **2020**, *12*, 1-6.

35. Zhu, K.; Wang, C.; Liu, J.; Wang, W.; Lv, Y.; Wang, P.; Meng, A.; Li, Z. Facile fabrication of ZnPc sensitized g-C3N4 through ball milling method toward an enhanced photocatalytic property. *J. Asian Ceram. Soc.* **2020**, *8*, 939-947.

36. Savio, A.K.P.D.; Fletcher, J.; Smith, K.; Iyer, R.; Bao, J.M.; Robles Hernández, F.C. Environmentally effective photocatalyst CoO-TiO₂ synthesized by thermal precipitation of Co in amorphous TiO₂. *Appl. Catal. B: Environ.* **2016**, *182*, 449-455.

37. Alvarez, L.; Almadori, Y.; Mariot, S.; Aznar, R.; Arenal, R.; Michel, T.; Le Parc, R.; Dieudonné, P.; Jousselme, B.; Campidelli, S.; Bantignies, J.L. New insights on photo-active molecules within host carbon nanotubes. *J. Nanolectron. Optoelectron.* **2013**, *8*, 28-35.

38. Das, N.M.; Singh, A.K.; Ghosh, D.; Bandyopadhyay, D. Graphene oxide nanohybrids for electron transfer mediated antimicrobial activity. *Nanoscale Adv.* **2019**, *1*, 3727-3740.

39. López, T.; Ortiz-Islands, E.; Guevara, P.; Rios, J.V. Preparation and characterization of copper compounds co-gelled with nanostructured TiO₂ materials to be used in cancer treatment. *Sci. Adv. Mater.* **2012**, *4*, 579-583.

40. Demir, F.; Yenilmez, H.Y.; Koca, A.; Bayır, Z.A. Synthesis, electrochemistry, and electrocatalytic activity of thiazole substituted phthalocyanine complexes. *J. Solid State Electrochem.* **2022**, *26*, 761-772.

41. Acar, I.; Bıyıklıoglu, Z.; Durmus, M.; Kantekin, H. Synthesis, characterization and comparative studies on the photophysical and photochemical properties of peripherally and non-peripherally tetra-substituted zinc(II) phthalocyanines. *J. Organomet. Chem.* **2012**, *708*, 65-74.

42. Thabet, R.H.; Alessa, R.E.M.; Al-Smadi, Z.K.K.; Alshatnawi, B.S.G.; Amayreh, B.M.I.; Al-Dwaaghreh, R.B.A.; Salah, S.K.A. Folic acid: Friend or foe in cancer therapy. *J. Int. Med. Res.* **2024**, *52*, 1-9.

43. Barrino, F. Hybrid organic-inorganic materials prepared by sol-gel and sol-gel-coating method for biomedical use: Study and synthetic review of synthesis and properties. *Coatings* **2024**, *14*, 1-19.

44. Zamojs, K.; Zdrowowicz, M.; Rudnicki-Velasquez, P.B.; Krzyminski, K.; Zaborowski, B.; Niedziałkowski, P.; Jacewicz, D.; Chmurzynska, L. The development of 1,3-diphenylisobenzofuran as a highly selective probe for the detection and quantitative determination of hydrogen peroxide. *Free Radic. Res.* **2017**, *51*, 38-46.

Disclaimer/Publisher's Note: The statements, opinions and data contained in all publications are solely those of the individual author(s) and contributor(s) and not of MDPI and/or the editor(s). MDPI and/or the editor(s) disclaim responsibility for any injury to people or property resulting from any ideas, methods, instructions or products referred to in the content.